
Tubular Riemannian Laplace Approximations for Bayesian Neural Networks

Rodrigo Pereira David¹

Abstract

Laplace approximations are among the simplest and most practical methods for approximate Bayesian inference in neural networks, yet their Euclidean formulation struggles with the highly anisotropic, curved loss surfaces and large symmetry groups that characterize modern deep models. Recent work has proposed Riemannian and geometric Gaussian approximations to adapt to this structure. Building on these ideas, we introduce the *Tubular Riemannian Laplace* (TRL) approximation. TRL explicitly models the posterior as a probabilistic tube that follows a low-loss valley induced by functional symmetries, using a Fisher/Gauss–Newton metric to separate prior-dominated tangential uncertainty from data-dominated transverse uncertainty. We interpret TRL as a scalable reparametrised Gaussian approximation that utilizes implicit curvature estimates to operate in high-dimensional parameter spaces. Our empirical evaluation on ResNet-18 (CIFAR-10 and CIFAR-100) demonstrates that TRL achieves excellent calibration, matching or exceeding the reliability of Deep Ensembles (in terms of ECE) while requiring only a fraction (1/5) of the training cost. TRL effectively bridges the gap between single-model efficiency and ensemble-grade reliability.

1. Introduction

Modern deep learning systems are increasingly deployed in safety-critical settings such as medical diagnosis, autonomous driving and scientific discovery. In these regimes, calibrated *uncertainty quantification* is as important as accuracy: models should know when they do not know (Gal, 2016; Kendall & Gal, 2017). Bayesian neural networks (BNNs) offer a principled way to reason about uncertainty

¹National Institute of Metrology, Technology and Quality (Inmetro). Correspondence to: Rodrigo Pereira Davi <rp-david@inmetro.gov>.

Preprint. Under review.

by placing priors over weights and maintaining a posterior distribution over parameters and induced functions (Rasmussen & Williams, 2006; Gal, 2016).

Unfortunately, exact Bayesian inference in deep networks is intractable, and practical Bayesian deep learning relies on approximate methods such as variational inference, Monte Carlo sampling, and Laplace approximations. Among these, the Laplace approximation remains attractive because it is conceptually simple, computationally cheap, and easy to integrate into existing training pipelines (Daxberger et al., 2021). The Euclidean Laplace approximation (ELA) fits a Gaussian in parameter space around the maximum a posteriori (MAP) estimate using the Hessian of the negative log-posterior. Despite recent advances in scalable Hessian approximation (Daxberger et al., 2021), ELA is known to underfit and produce poorly calibrated uncertainty for deep networks.

A recent line of work addresses part of this problem by moving from parameter space to function space. The *linearised Laplace approximation* (LLA) linearises the network around the MAP and propagates a Gaussian weight posterior through the Jacobian, yielding a Gaussian process in function space that better captures predictive uncertainty (e.g. Daxberger et al., 2021; Roy et al., 2024). At the same time, information geometry and Riemannian optimisation have highlighted that neural network parameter spaces carry rich geometric structure when equipped with metrics derived from the Fisher information or Gauss–Newton matrices (Amari, 1998; Bonnabel, 2013; Kristiadi et al., 2023). This has led to *Riemannian Laplace approximations* (RLA) that sample from approximate posteriors using geodesic flows with respect to such metrics (Bergamin et al., 2023; Yu et al., 2024).

A complementary perspective comes from Da Costa et al. (2025), who introduce *geometric Gaussian approximations* and show that families of posterior approximations obtained by pushing forward Gaussian base measures through diffeomorphisms (ReparamGA) or Riemannian exponential maps (RiemannGA) are universal under mild regularity conditions. This unifies many existing Laplace-like methods under a common geometric umbrella, and clarifies the role of the metric and parametrisation.

This paper. We build on these advances and propose the *Tubular Riemannian Laplace* (TRL) approximation, a geometric posterior approximation tailored to Bayesian neural networks. TRL is motivated by two empirical observations about deep networks: (i) the posterior mass is often organised along high-dimensional *loss valleys* or tunnels (Dold et al., 2025) generated by functional symmetries in weight space, (ii) the curvature of the negative log-posterior is extremely anisotropic, with nearly flat directions along these valleys and sharp directions across them. Standard Gaussian approximations are ill-suited to this geometry: fitting an ellipsoid to a long, curved valley is inherently inadequate.

Instead of a single Gaussian “bubble” centred at the MAP, TRL models the approximate posterior as a *probabilistic tube* that follows a low-loss curve through parameter space. The tube has three key ingredients: (i) an axis given by a curve that traces an approximate invariance valley, (ii) a transverse covariance determined by the Fisher/Gauss–Newton metric, and (iii) a tangential variance governed primarily by the prior. Sampling from the tube is implemented as a pushforward of an isotropic Gaussian in a latent space containing a one-dimensional valley coordinate and transversal coordinates.

We make the following contributions:

- We introduce *Tubular Riemannian Laplace* (TRL), a geometric posterior approximation that models posterior mass as a probabilistic tube along symmetry-induced low-loss valleys, separating prior-dominated tangential uncertainty from data-dominated transverse uncertainty under a Fisher/Gauss–Newton metric.¹
- We derive a scalable implementation combining a stochastic spine construction with implicit curvature estimation via Lanczos and Hessian–vector products, enabling TRL to operate in high-dimensional networks without explicit Hessian or Jacobian materialization, at cost comparable to standard training.
- We provide an empirical evaluation ranging from synthetic manifolds to ResNet-18 on CIFAR-100 (main) and CIFAR-10 (Appendix B.3). TRL achieves strong calibration in high-dimensional regimes, matching Deep Ensembles in ECE while requiring only a fraction (1/5) of the training cost.

Throughout, we focus on the geometric formulation and algorithmic design of TRL, providing empirical validation on standard benchmarks to demonstrate its efficacy in calibration and out-of-distribution detection.

¹Code is available at <https://github.com/rpdavid78/trl-experiments>

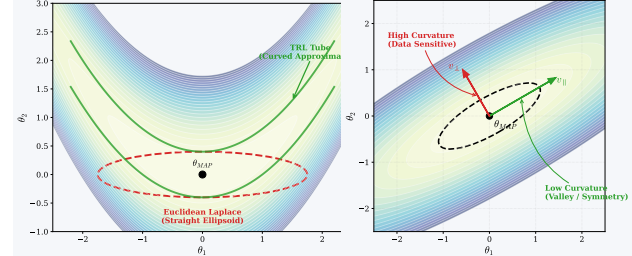


Figure 1. Geometry of TRL. (a) Euclidean Laplace fits a local ellipsoid, while TRL models the posterior as a tube along the low-loss valley. (b) We decompose curvature into invariance (v_{\parallel}) and data-sensitive (v_{\perp}) directions.

2. Background

We consider a Bayesian Neural Network with prior $p(\theta)$ and likelihood $p(\mathcal{D} | \theta)$. Standard approximations include the *Euclidean Laplace Approximation* (ELA), which fits a Gaussian $\mathcal{N}(\theta_{\text{MAP}}, H^{-1})$ at the mode, and the *Linearised Laplace Approximation* (LLA), which applies this Gaussian to the first-order Taylor expansion of the network function. We refer readers unfamiliar with these methods or with the Fisher Information Matrix $F(\theta)$ to [Appendix A.1](#).

3. Geometry of loss valleys in deep networks

In deep networks, the geometry of $L(\theta)$ is characterised by two key features:

1. **Symmetry-induced valleys.** Many parameter configurations implement the same function f_{θ} due to symmetries (e.g., permutations, scaling). These generate orbits in weight space along which the loss remains essentially constant, forming high-dimensional valleys (Garipov et al., 2018; Draxler et al., 2018).
2. **Extreme anisotropy of curvature.** The loss is extremely flat along symmetry directions and steep along data-sensitive directions. The Hessian spectrum thus exhibits a wide range of eigenvalues, with a bulk of near-zero values (Sagun et al., 2017; Maddox et al., 2019).

Figure 1(a) illustrates this in a simple two-dimensional toy landscape: the posterior mass concentrates along a curved low-loss valley, yet a single Euclidean Gaussian ellipsoid must either be too narrow across the valley (missing most of the mass) or too wide along it (spilling into high-loss regions). This geometric mismatch is the starting point for TRL, which replaces the ellipsoid by a tube aligned with the valley.

3.1. Fisher-based tangent/normal decomposition

Let $\theta_0 = \theta_{\text{MAP}}$, and let $F_0 = F(\theta_0)$ be the Fisher information matrix evaluated at the MAP. We consider the

regularised metric

$$G_0 = F_0 + \lambda I, \quad (1)$$

which combines the data–driven curvature with the isotropic prior.

We define an approximate decomposition of the tangent space $T_{\theta_0} \Theta$ into

$$T_{\theta_0} \Theta = T_{\theta_0} \oplus N_{\theta_0}, \quad (2)$$

where:

- T_{θ_0} is spanned by directions v for which $v^\top F_0 v \approx 0$, i.e., directions along which the network function (and thus the likelihood) changes very little. These are approximate invariance or symmetry directions.
- N_{θ_0} is the G_0 -orthogonal complement, spanned by directions along which $v^\top F_0 v$ is large, i.e., directions that significantly affect the function and are strongly constrained by the data.

Figure 1(b) shows a two-dimensional cartoon of this decomposition: the valley direction v_{\parallel} lies along the bottom of the loss valley, where the Fisher curvature is negligible, while a transverse direction v_{\perp} points across the valley and is associated with large Fisher eigenvalues. In TRL, v_{\parallel} defines the tube axis and the columns of N_{θ_0} define the transverse directions used to model the tube width.

In practice we approximate this decomposition via the eigen-decomposition of G_0 . Let $G_0 = U \Lambda U^\top$ with eigenvalues $0 < \lambda_1 \leq \lambda_2 \leq \dots \leq \lambda_K$. We choose the smallest eigenvector $v_{\parallel} = u_1$ as a representative valley direction, and a set of k principal transverse directions $N_0 = [u_{i_1}, \dots, u_{i_k}]$ corresponding to large eigenvalues. This yields a low-dimensional approximation

$$T_{\theta_0} \approx \text{span}\{v_{\parallel}\}, \quad N_{\theta_0} \approx \text{span}\{N_0\}. \quad (3)$$

3.2. Prior- vs data-dominated variance

Under a Gaussian approximation with precision matrix $H \approx F_0 + \lambda I$, the variance along an eigenvector u_i is approximately $1/(\lambda_i(F_0) + \lambda)$. Thus:

- For tangential directions with $\lambda_i(F_0) \approx 0$, the variance is dominated by the prior, $\text{Var}_{\parallel} \approx 1/\lambda$.
- For transverse directions with $\lambda_i(F_0) \gg \lambda$, the variance is dominated by the data, $\text{Var}_{\perp} \approx 1/\lambda_i(F_0)$.

This simplified picture clarifies the core difficulty for Euclidean Laplace: any single ellipsoid cannot simultaneously be narrow in data-sensitive directions and wide enough along a long, curved valley of functional symmetries. TRL directly addresses this mismatch by abandoning a single local ellipsoid in favour of a tube that follows the valley.

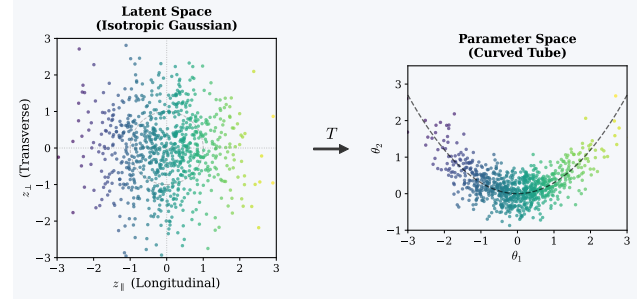


Figure 2. TRL as a tubular pushforward. Left: samples from an isotropic Gaussian in latent coordinates $(z_{\parallel}, z_{\perp})$. Right: the corresponding samples in parameter space under a tubular map T , forming a curved tube along a low-loss valley.

4. Tubular Riemannian Laplace approximation

We now introduce the Tubular Riemannian Laplace (TRL) approximation. Our goal is to construct an approximate posterior that: (i) follows a low-loss valley induced by functional symmetries, (ii) reflects data-driven curvature in directions transverse to the valley via the Fisher/Gauss–Newton metric, and (iii) remains computationally comparable to Euclidean and linearised Laplace methods.

Figure 2 provides an intuitive two-dimensional illustration of TRL as a reparametrised Gaussian approximation. A simple isotropic Gaussian in latent tubular coordinates $(z_{\parallel}, z_{\perp})$ is mapped by a non-linear tubular map T into parameter space, producing a tube-shaped distribution that follows a curved valley rather than a single local ellipsoid.

4.1. Setup and notation

Let $\theta_0 = \theta_{\text{MAP}}$ and $F_0 = F(\theta_0)$, $G_0 = F_0 + \lambda I$ as in Section 3. We extract:

- A valley direction $v_{\parallel} \in \mathbb{R}^K$ as the normalised eigenvector of G_0 associated with the smallest eigenvalue λ_{\parallel} .
- A $K \times k$ matrix N_0 whose columns form an orthonormal basis (with respect to G_0) of a k -dimensional transverse subspace N_{θ_0} , typically chosen as the top- k eigenvectors of G_0 that are orthogonal to v_{\parallel} .

We also define a transverse precision matrix

$$H_{\perp} = N_0^\top H_0 N_0, \quad (4)$$

where H_0 is a suitable Hessian or Gauss–Newton approximation at θ_0 . The corresponding covariance is $\Sigma_{\perp} = H_{\perp}^{-1}$, and we denote its Cholesky factor by L_{\perp} with $\Sigma_{\perp} = L_{\perp} L_{\perp}^\top$.

4.2. Curvature metric selection.

While we denote the local curvature at step t by H_t , strict adherence to the exact Hessian is problematic in deep learning: the loss landscape is highly non-convex, and negative eigenvalues would render the transverse covariance $\Sigma_{\perp,t}$ ill-defined. In practice, we therefore employ positive semi-definite (PSD) approximations of curvature, such as the Generalized Gauss–Newton (GGN) matrix or a rectified Hessian obtained by clamping eigenvalues to a small positive threshold. Both choices ensure that the induced covariance in the transverse subspace admits a valid probabilistic interpretation.

The GGN has become the de facto standard in the Laplace-approximation literature because it provides a sound approximation to the Fisher information metric while remaining computationally stable and amenable to Kronecker factorizations (Martens & Grosse, 2015; Daxberger et al., 2021). In contrast, the empirical Fisher—which replaces the true data distribution by the empirical one—can lead to severely distorted curvature estimates and unstable natural-gradient updates, as rigorously demonstrated by Kunstner et al. (2019). By building TRL on top of GGN-style metrics (or, at worst, a PSD-rectified Hessian), we inherit these theoretical guarantees: the transverse covariance $\Sigma_{\perp,t}$ is always well-defined, and the dominant directions in \mathcal{N}_t align with directions where the data genuinely constrains the model, rather than artifacts of an ill-behaved curvature approximation.

4.3. Valley curve and tubular coordinates

The idealised TRL assumes the existence of a smooth curve

$$\gamma : \mathbb{R} \rightarrow \mathbb{R}^K, \quad t \mapsto \gamma(t), \quad (5)$$

through parameter space such that:

$$\gamma(0) = \theta_0, \quad (6)$$

$$L(\gamma(t)) \approx L(\theta_0) \quad \text{for } t \text{ in a suitable interval}, \quad (7)$$

$$\dot{\gamma}(t) = \frac{d}{dt} \gamma(t) \in T_{\gamma(t)} \Theta \quad (8)$$

and $\dot{\gamma}(t)$ approximately spans the low-Fisher-curvature directions, i.e., $\dot{\gamma}(t)^\top F(\gamma(t)) \dot{\gamma}(t) \approx 0$. In practice, we consider approximations of this curve, as discussed in Section 4.5.

We now define *tubular coordinates* $(z_{\parallel}, z_{\perp})$, where:

- $z_{\parallel} \in \mathbb{R}$ is a scalar coordinate along the valley direction.
- $z_{\perp} \in \mathbb{R}^k$ are transverse coordinates in the span of N_0 .

We will use a scaling factor $\alpha > 0$ to map valley coordinates to physical distances along γ . Heuristically, to match the

prior-dominated variance along the valley, we set

$$\alpha \approx \frac{1}{\sqrt{\lambda}}, \quad (9)$$

so that if $z_{\parallel} \sim \mathcal{N}(0, 1)$ then the variance of the induced displacement along the valley is approximately $1/\lambda$.

4.4. The tubular map and TRL posterior

The TRL approximation is defined via a map

$$T : \mathbb{R}^{1+k} \rightarrow \mathbb{R}^K, \quad (10)$$

$$(z_{\parallel}, z_{\perp}) \mapsto w = T(z_{\parallel}, z_{\perp}). \quad (11)$$

In its most general form we set

$$T(z_{\parallel}, z_{\perp}) = \gamma(\alpha z_{\parallel}) + N(\alpha z_{\parallel}) L_{\perp}(\alpha z_{\parallel}) z_{\perp}, \quad (12)$$

where:

- $N(t)$ is a $K \times k$ matrix whose columns form an orthonormal basis of the transverse subspace $N_{\gamma(t)}$ with respect to the local metric $G(\gamma(t))$.
- $L_{\perp}(t)$ is a Cholesky factor of the transverse covariance $\Sigma_{\perp}(t)$, typically defined via a projected Hessian at $\gamma(t)$.

Defining a standard Gaussian on the latent space,

$$z = (z_{\parallel}, z_{\perp}) \sim \mathcal{N}(0, I_{1+k}), \quad (13)$$

we obtain the TRL approximate posterior as the pushforward

$$q_{\text{TRL}}(w) = T_* \mathcal{N}(0, I_{1+k}). \quad (14)$$

By construction, q_{TRL} is a reparametrised Gaussian approximation (ReparamGA) in the sense of Da Costa et al. (2025), with the tubular map T chosen to align with low-loss valleys and Fisher-defined transverse directions. Crucially, we treat q_{TRL} as an *implicit* approximate posterior. The density could in principle be evaluated via the change-of-variables formula (requiring the costly Jacobian determinant of T) however, we bypass this step. Our primary goal is uncertainty quantification via Monte Carlo estimates of predictive moments (Eqs. (15)–(16)), where sampling from the tubular pushforward is sufficient and computationally efficient, avoiding explicit density or evidence evaluation.

Sampling and prediction. To sample from TRL and compute predictive statistics:

1. Sample S latent vectors $z^{(s)} = (z_{\parallel}^{(s)}, z_{\perp}^{(s)}) \sim \mathcal{N}(0, I_{1+k})$.
2. Map each latent sample to weights via $w^{(s)} = T(z^{(s)})$.

3. Evaluate the non-linear network $y_{\star}^{(s)} = f_{w^{(s)}}(x_{\star})$.
4. Approximate predictive mean and variance via Monte Carlo:

$$\hat{\mu}_{\star} = \frac{1}{S} \sum_{s=1}^S y_{\star}^{(s)}, \quad (15)$$

$$\widehat{\text{Var}}(y_{\star} \mid x_{\star}, \mathcal{D}) = \frac{1}{S} \sum_{s=1}^S \|y_{\star}^{(s)} - \hat{\mu}_{\star}\|^2. \quad (16)$$

Unlike LLA, TRL keeps the full non-linear network for prediction, while sampling from a geometrically informed posterior.

Algorithm 1 Practical TRL Inference

Require: MAP θ_{MAP} , step Δs , length T , rank k_{\perp} , scale β_{\perp} , corr. η_{corr} .

- 1: **Initialize:** Spine $\gamma_0 \leftarrow \theta_{\text{MAP}}$.
- 2: Construct basis N_0 from top- k_{\perp} eigenvectors via **Lanczos iteration** using implicit Hessian-vector products.
- 3: *% Stage A: Tube Construction*
- 4: **for** $t = 0$ to $T - 1$ **do**
- 5: Estimate valley tangent $v_{\parallel, t}$ (smallest eigenvector of G_t) via Lanczos iteration.
- 6: **Update Spine:** $\gamma_{t+1} \leftarrow \gamma_t + \Delta s v_{\parallel, t} - \eta_{\text{corr}}(I - v_{\parallel, t} v_{\parallel, t}^{\top}) \nabla_{\theta} \mathcal{L}(\gamma_t)$.
- 7: **Parallel Transport:** Transport $N_t \rightarrow N_{t+1}$ and orthonormalize wrt H_t .
- 8: Compute scale factor $L_{\perp, t}$ via Cholesky of projected curvature.
- 9: Store tube element $\mathcal{T}_t = \{\gamma_t, N_t, L_{\perp, t}\}$.
- 10: **end for**
- 11: *% Stage B: Sampling & Prediction*
- 12: **for** $s = 1$ to S **do**
- 13: Sample latent coordinates: $z_{\parallel} \sim \mathcal{N}(0, 1)$, $z_{\perp} \sim \mathcal{N}(0, I_{k_{\perp}})$.
- 14: Map z_{\parallel} to discrete spine index t .
- 15: **Map to Weight:** $\theta^{(s)} \leftarrow \gamma_t + N_t(\beta_{\perp} L_{\perp, t} z_{\perp})$
- 16: **if** Network uses Batch Normalization **then**
- 17: Forward pass on training subset to recalibrate BN stats for $\theta^{(s)}$.
- 18: **end if**
- 19: Compute output $y^{(s)} \leftarrow f(x_{\star}; \theta^{(s)})$.
- 20: **end for**
- 21: **return** Predictive mean $\hat{\mu}_{\star} = \frac{1}{S} \sum y^{(s)}$ and variance.

The general tubular map in Eq. (12) assumes access to (i) a smooth valley curve $\gamma(t)$, (ii) parallel transport of transverse bases along this curve, and (iii) position-dependent transverse covariances. Computing all of this exactly would require solving coupled differential equations in parameter

space and recomputing curvature continuously, which is prohibitive for modern neural networks.

In our experiments we therefore approximate this continuous geometry with a discrete, Hessian-based construction that can be implemented efficiently on top of a standard Laplace object. The idea is to replace the continuous valley $\gamma(t)$ by a finite, ordered set of parameter states that sample the low-loss region. We refer to this one-dimensional sequence of points as a *spine* of the valley: it plays the role of a discretised centreline of the tubular posterior. Small step sizes and a sufficient number of points yield a good approximation to the ideal continuous curve, while keeping the computational cost comparable to that of Euclidean or linearised Laplace.

4.5. Practical TRL implementation

To make TRL tractable for deep networks, we implement a discretised approximation of the tubular geometry using a corrective spine and discrete parallel transport. The construction replaces the continuous ODEs with a robust predictor-corrector scheme that tracks the low-loss valley while maintaining an orthonormal transverse coordinate system. To scale to millions of parameters, we employ the Lanczos algorithm with implicit Hessian-vector products and robust RMS-gradient normalization to prevent numerical instability in steep valleys (details in Appendix A.3). The resulting inference scheme, mathematically derived in Appendix A.2, is summarized in Algorithm 1.

Dimensionality reduction via low-rank curvature. Ideally, the transverse subspace \mathcal{N}_t would span the entire orthogonal complement. However, the Hessian spectrum of neural networks is dominated by a few large eigenvalues (Maddox et al., 2019). By selecting a small k_{\perp} based on the leading eigenvectors (computed via Lanczos iteration), TRL captures the *stiff* directions where the data imposes strong constraints. This yields linear memory complexity $O(T \cdot K \cdot k_{\perp})$, avoiding the $O(K^2)$ cost of full Hessian storage, with minimal loss of predictive variance.

Sampling. We sample in latent tubular coordinates $(z_{\parallel}, z_{\perp}) \sim \mathcal{N}(0, I)$ and map to parameter space via $\theta = \gamma_t + N_t(\beta_{\perp} L_{\perp, t} z_{\perp})$. Here, β_{\perp} allows calibration of the tube width relative to the local curvature. The discrete spine index t is mapped from z_{\parallel} to cover the valley length defined by the prior scale α . This yields a computationally efficient sampling scheme that respects the local geometry (via $L_{\perp, t}$) while remaining linear in the subspace rank k_{\perp} .

Remark on Spine Dimensionality. While the invariance manifold may be high-dimensional, we explicitly model a 1D spine to maintain a tractable intrinsic parameterization. Crucially, assuming a 1D spine does not imply the invari-

ance manifold is strictly one-dimensional. If the low-loss region is higher-dimensional (e.g., a 2D sheet), the primary direction of motion is captured by the spine $\gamma(t)$, while orthogonal flat directions are naturally captured by the transverse covariance $\Sigma_{\perp,t}$. Since $\Sigma_{\perp,t}$ is derived from the local curvature, directions with near-zero eigenvalues orthogonal to the spine result in large variance, effectively modeling a “flattened tube” that covers the multi-dimensional manifold.

Batch Normalization Recalibration. To mitigate covariate shift caused by sampling weights far from the mode, we implement *FixBN*: for each sample $\theta^{(s)}$, we recalibrate the batch statistics via a single forward pass on a clean training subset (details in Appendix B.2).

5. Relation to existing methods

Euclidean vs tubular Laplace. Euclidean Laplace assumes that a single Gaussian in Euclidean parameter space is adequate. TRL replaces this with a Gaussian in latent *tubular* coordinates, mapped non-linearly to parameter space. Along the valley direction, variance is primarily controlled by the prior through α ; across the valley, variance follows the Fisher/Hessian curvature. This directly addresses the tension between narrow cross-valley directions and wide symmetry directions that ELA cannot resolve.

Linearised Laplace. LLA linearises the network around the MAP and effectively projects uncertainty onto the function space tangent at θ_0 . TRL instead keeps the full non-linearity but restricts samples to a geometrically informed tube. In regimes where the network is approximately linear along the valley, TRL and LLA may behave similarly, but TRL can in principle capture non-linear effects along invariance directions that LLA linearisation discards.

Riemannian Laplace. Bergamin et al. (2023) use a Monge-type metric to define an ODE that transports Gaussian samples through curved parameter space. Yu et al. (2024) improve this with Fisher metrics and volume corrections but require expensive log-determinant computations. TRL adopts a Fisher/Gauss–Newton metric to identify tangential and transverse directions but avoids the cost of solving geodesic ODEs *during inference for every sample*. Instead, TRL pre-computes the dominant geometric structure (the spine) once. This reduces sampling to a simple linear projection, offering massive speedups over ODE-based samplers (see Appendix D for a detailed complexity analysis) while capturing the anisotropic structure.

Riemannian diffusions and functional invariances. (Roy et al., 2024) show that lack of reparameterization invariance is a key weakness of many approximate posteriors, and propose Riemannian diffusion processes that sample

in spaces that quotient out symmetry directions, yielding posteriors invariant at the level of functions. TRL is conceptually aligned with this view in that it treats symmetry directions as the primary source of geometric difficulty and explicitly parameterises a tube along a valley of approximate symmetries. However, it does not implement a diffusion or enforce exact invariance; it provides a deterministic tubular parametrisation that is simpler to implement and reason about.

Geometric Gaussian approximations. Within the framework of Da Costa et al. (2025), TRL is a ReparamGA with a specific choice of tubular diffeomorphism T . Under flat metrics, ReparamGA and RiemannGA coincide, so TRL can also be seen as a Riemannian Gaussian approximation with a metric chosen to align with Fisher/Gauss–Newton curvature. The universality results for ReparamGA justify the search for geometric approximations. While theoretical frameworks for coordinate-invariant Laplace exist (Léger & Vialard, 2024), TRL focuses on a scalable tubular implementation tailored to the anisotropic curvature of neural networks.

Post-hoc parameter-space inference vs. function-space priors. Unlike methods that enforce explicit function-space priors during training, such as Gaussian processes (Rasmussen & Williams, 2006) or particle inference methods like FSP-Laplace (Cinquin et al., 2024; Sun et al., 2019), TRL does not require modifying the optimization objective. Function-space approaches typically introduce a regularization term (e.g., KL divergence to a GP) to enforce reversion to the prior mean far from data, often forcing a compromise between data fit and prior adherence that can degrade MAP accuracy. TRL, in contrast, is a fully post-hoc parameter-space method: the prior acts on weights, encoding structural simplicity rather than locality, leaving the MAP network unchanged. The tubular construction inherits the network’s extrapolation behavior along the invariance valley, capturing complex non-local symmetries while forgoing strict “revert-to-prior” guarantees. In this sense, TRL prioritizes geometric fidelity over asymptotic function-space constraints, effectively decoupling training performance from the uncertainty quantification mechanism.

6. Experiments

Experimental Setup. To ensure a controlled comparison, we keep the architecture and MAP training protocol fixed (ResNet-18) across methods. Post-hoc approaches (ELA, LLA (Daxberger et al., 2021), and TRL) are applied to the same pretrained MAP checkpoint, and SWAG (Maddox et al., 2019) is initialized from this checkpoint. Training-based baselines include Deep Ensembles (Lakshminarayanan et al., 2017) (with $M = 5$ independently

trained models) and MC Dropout (Gal & Ghahramani, 2016) (trained with dropout enabled).

We decouple prior selection from method-specific hyperparameters. For Laplace-based methods (ELA, LLA, TRL), we optimize the prior precision via marginal likelihood, following Immer et al. (2021) as a scalable alternative to cross-validation in high-dimensional settings. For training-based baselines, we use standard literature configurations (e.g., $M = 5$ for ensembles and dropout probability $p = 0.1$ for MC Dropout). TRL introduces additional geometric hyperparameters (e.g., tube scale β_{\perp} and spine length T), which we select via validation-set grid search minimizing NLL. Full details and search spaces are provided in Appendix B.

6.1. Scalability to High-dimensional Vision Tasks

Building on the validation in toy manifolds against exact Full-Network Laplace baselines (Appendix C), we now evaluate TRL on a significantly more challenging benchmark: ResNet-18 on CIFAR-100. This setting introduces high-dimensional non-convexity (~ 11 million parameters) combined with data scarcity per class, creating a landscape with steep curvature that severely tests the stability of geometric approximations.

Setup.

We adapt the standard ResNet-18 architecture by replacing the initial 7×7 convolution with a 3×3 kernel (stride 1) to preserve spatial resolution. To ensure a fair comparison, we train the MAP solution for 50 epochs using SGD with cosine annealing, achieving a test accuracy of 74.22%. For Laplace baselines, we employ the Last-Layer Euclidean (ELA) and Linearised (LLA) approximations. For LLA, we use the standard Generalized Linear Model (GLM) formulation with analytic Probit approximation. Full-network LLA requires forming Jacobians of the network outputs with respect to a large subset of parameters, which is memory- and compute-prohibitive beyond the last layer in modern CNNs. In contrast, TRL relies on Hessian–vector products and low-rank curvature information along a one-dimensional spine, and does not require explicit Jacobian construction. Therefore, we evaluate LLA/ELA in the feasible last-layer setting and use toy-scale models to additionally compare against full-network Laplace baselines where they are tractable. Given the high dimensionality of the CIFAR-100 readout layer ($|\theta_{\text{last}}| \approx 51,200$), even the exact last-layer Hessian becomes memory-prohibitive; thus, we utilize a Kronecker-factored (Kron) curvature approximation (Daxberger et al., 2021) with prior precision optimized via marginal likelihood. We compare against strong training-based baselines: SWAG, MC Dropout, and the gold-standard Deep Ensembles ($M = 5$). Detailed configurations for all baselines are provided in Appendix B.5.

Prior and Regularization. Operating on the full parameter space of ResNet-18 requires overcoming numerical instabilities caused by highly anisotropic curvature. We implement a robust layer-wise strategy detailed in Appendix B.2: we optimize the prior precision of the linear head via marginal likelihood ($\lambda_{\text{head}} \approx 5.3$) but impose a stronger regularization on the convolutional backbone using a boost factor $\gamma = 50$ ($\lambda_{\text{body}} \approx 265$). This improves stability while preserving flexibility in the classifier.

TRL Configuration. We construct the tubular posterior using implicit Hessian–vector products via Lanczos iterations with memory-efficient CPU offloading. To prevent instability in steep transverse directions, we replace raw gradient steps with an RMS-normalized update rule. We set the transverse rank to $k_{\perp} = 30$ to capture a broader subspace of the curvature spectrum. Based on grid search validation, we selected a spine length of $T = 40$ steps with a step size $\Delta s = 0.01$ and a tube scale factor $\beta_{\perp} = 4.0$. Batch Normalization statistics are handled by recalibrating on a clean subset of training data without augmentation for each posterior sample (“FixBN”) using $S = 25$ Monte Carlo samples.

Results We first evaluate the validity of the Gaussian assumption in this high-dimensional regime ($|\theta_{\text{last}}| \approx 51,200$). Table 1 reveals a failure of static Laplace baselines. A single Gaussian ellipsoid centered at the mode forces a dilemma: if it is tight, it underestimates predictive uncertainty; if it is wide enough to cover curvature, it inevitably spills probability mass into high-loss regions, leading to severe miscalibration. While replacing the analytic Probit with Monte Carlo integration improves LLA in this regime (NLL $1.42 \rightarrow 1.28$, ECE $0.34 \rightarrow 0.24$, see Appendix B.5.1), the static Gaussian assumption remains fundamentally limiting, and performance stays far from TRL (NLL 0.95, ECE 0.017). TRL addresses this by transporting the distribution mean along the invariance manifold, decoupling functional diversity from local curvature. The computationally heavy steps are performed offline when constructing the spine; at inference time, the online cost reduces to matrix–vector products and standard forward passes, and our FixBN procedure follows the practice adopted in SWAG.

Precision vs. Averaging: TRL vs. SWAG. A key finding is TRL’s superiority over SWAG in likelihood modeling (NLL **0.9525** vs. 1.0055). While SWAG constructs a Gaussian approximation by averaging moments over the SGD trajectory, this effectively fits a convex ellipsoid to a potentially non-convex, curved path. If the trajectory traces a “banana” shape, SWAG’s approximation inevitably includes high-loss regions in the center of the curve (overestimating variance in orthogonal directions). TRL, conversely, strictly parameterises the low-loss curve. By defining uncertainty via a geodesic tube rather than a global average, TRL re-

Table 1. Benchmark on CIFAR-100 (ResNet-18). TRL achieves ensemble-level calibration (ECE) from a single MAP-trained backbone, notably outperforming SWAG and MC Dropout in NLL and calibration metrics. TRL narrows the gap to the Deep Ensemble gold standard without training multiple models.

METHOD	IN-DISTRIBUTION (CIFAR-100)				OOD (SVHN) AUROC \uparrow
	ACC \uparrow	NLL \downarrow	ECE \downarrow	BRIER \downarrow	
<i>Gold Standard (High Cost)</i>					
DEEP ENSEMBLES	78.36%	0.7919	0.0161	0.3032	0.8843
<i>Training-based Baselines</i>					
SWAG	75.29%	1.0055	0.0917	0.3572	0.8033
MC DROPOUT	74.83%	1.0124	0.0894	0.3630	0.8226
<i>Post-hoc Baselines</i>					
MAP	74.22%	1.0358	0.0946	0.3689	0.8028
ELA (LAST-LAYER)	72.83%	1.3433	0.2626	0.4654	0.8451
LLA-GLM (LAST-LAYER)	73.91%	1.4787	0.3636	0.5164	0.8740
TRL (OURS)	74.51%	0.9525	0.0171	0.3533	0.8255

mains faithful to the underlying manifold. This geometric fidelity translates directly to better uncertainty quantification, achieving lower entropy on reliable predictions and better separation of distinct functional modes.

Ensemble-Grade Calibration at Single-Model Cost. Perhaps the most significant result is the calibration performance. TRL achieves an ECE of **0.0171**, virtually indistinguishable from the $5 \times$ costlier Deep Ensemble (0.0161) and $5 \times$ better than SWAG (0.0917). This suggests a fundamental insight: much of the calibration gain in Ensembles comes from sampling diverse solutions along the loss landscape. TRL demonstrates that exploring a *single* connected basin with high geometric precision yields equivalent calibration benefits to training multiple independent models, but within a $1 \times$ training budget (with a linear storage overhead for the spine, see Appendix D). This effectively closes the gap between post-hoc Laplace methods and expensive ensembling techniques for in-distribution reliability.

While TRL achieves excellent in-distribution calibration (ECE), its OOD detection performance (AUROC) is competitive but slightly lower than linearized baselines. This suggests that TRL prioritizes geometric fidelity to the parameter-space posterior (yielding high calibration) over the asymptotic function-space behavior, a trade-off we further discuss in Section 7.

Our method achieves superior reliability among single-model baselines in this high-dimensional regime. By explicitly modeling the non-linear manifold, TRL mitigates the underfitting of static Laplace approximations and outperforms training-based methods such as SWAG. Additional robustness analyses and hyperparameter details for CIFAR-100 are in Appendix B.4, with consistent CIFAR-10 results in Appendix B.3.

7. Conclusion

We have introduced the Tubular Riemannian Laplace (TRL) approximation, a geometric method for Bayesian neural networks that explicitly models the posterior mass as a probabilistic tube following low-loss valleys. By decomposing the parameter space into prior-dominated tangential directions and data-dominated transverse directions, TRL overcomes the geometric limitations of static Gaussian approximations (ELA/LLA), which struggle to capture the curved, anisotropic structure of modern loss landscapes.

Our experimental evaluation demonstrates that this geometric fidelity translates into tangible performance gains. On controlled benchmarks, TRL eliminates the pathologies of underfitting and over-conservatism. Crucially, we showed that the method scales to high-dimensional deep learning, effectively bridging the gap between single-model efficiency and ensemble-grade reliability.

Finally, bridging parameter-space geometry with asymptotic function-space safety guarantees remains an open frontier. Future work could leverage TRL’s efficient valley traversal to propose particles for hybrid function-space inference. Furthermore, while we demonstrate scalability to 11M parameters, applying curvature-based methods to billion-scale transformers represents a significant computational challenge for future research.

Impact Statement

This work advances safe deployment in critical domains by improving reliability via geometric inference. While TRL mitigates overconfident failures through better calibration, it does not correct inherent data biases; practitioners must remain mindful of these limitations in high-stakes contexts.

References

Amari, S.-i. Natural gradient works efficiently in learning. *Neural Computation*, 10(2):251–276, 1998.

Antorán, J., Janz, D., Allingham, J. U., Daxberger, E., Barbano, R., Nalisnick, E., and Hernández-Lobato, J. M. Adapting the linearised laplace model evidence for modern deep learning. In *International Conference on Machine Learning*, pp. 796–821. PMLR, 2022.

Bergamin, F., Moreno-Muñoz, P., Hauberg, S., and Arvanitidis, G. Riemannian laplace approximations for bayesian neural networks. In *Advances in Neural Information Processing Systems*, 2023.

Bonnabel, S. Stochastic gradient descent on riemannian manifolds. *IEEE Transactions on Automatic Control*, 58(9):2217–2229, 2013.

Cinquin, C., Ober, S. W., Ruegamer, D., Koehler, J., and Fortuin, V. FSP-Laplace: Function-space priors for the Laplace approximation in Bayesian deep learning. In *Advances in Neural Information Processing Systems*, volume 37, 2024.

Da Costa, N., Mucsányi, B., and Hennig, P. Geometric gaussian approximations of probability distributions. *arXiv preprint arXiv:2507.00616*, 2025.

Daxberger, E., Kristiadi, A., Immer, A., Eschenhagen, R., Bauer, M., and Hennig, P. Laplace redux: Effortless Bayesian deep learning. In *Advances in Neural Information Processing Systems (NeurIPS)*, 2021.

Dold, D., Kobialka, J., Palm, N., Sommer, E., Rügamer, D., and Dürr, O. Paths and ambient spaces in neural loss landscapes. 258:10–18, 03–05 May 2025. URL <https://proceedings.mlr.press/v258/dold25a.html>.

Draxler, F., Veshchikov, K., Gundlach, M., Widmer, D., Scheck, I., and Seveljet, T. Essentially no barriers in neural network energy landscape. *International Conference on Machine Learning (ICML)*, 2018.

Gal, Y. *Uncertainty in Deep Learning*. PhD thesis, University of Cambridge, 2016.

Gal, Y. and Ghahramani, Z. Dropout as a bayesian approximation: Representing model uncertainty in deep learning. In *international conference on machine learning*, pp. 1050–1059. PMLR, 2016.

Garipov, T., Izmailov, P., Podoprikhin, D., Vetrov, D. P., and Wilson, A. G. Loss surfaces, mode connectivity, and fast ensembling of DNNs. In *Advances in Neural Information Processing Systems (NeurIPS)*, 2018.

Immer, A., Bauer, M., Fortuin, V., Rätsch, G., and Khan, M. E. Scalable marginal likelihood estimation for model selection in deep learning. In *International Conference on Machine Learning (ICML)*, 2021.

Kendall, A. and Gal, Y. What uncertainties do we need in bayesian deep learning for computer vision? In *Advances in Neural Information Processing Systems*, 2017.

Kristiadi, A., Daxberger, E., and Hennig, P. The geometry of neural networks’ parameter spaces under reparametrization. *Advances in Neural Information Processing Systems*, 2023.

Kunstner, F., Balles, L., and Hennig, P. Limitations of the empirical fisher approximation for natural gradient descent. In *Advances in Neural Information Processing Systems (NeurIPS)*, 2019.

Lakshminarayanan, B., Pritzel, A., and Blundell, C. Simple and scalable predictive uncertainty estimation using deep ensembles. In *Advances in Neural Information Processing Systems*, volume 30, 2017.

Léger, F. and Vialard, F.-X. A geometric Laplace method. In *Proceedings of The 27th International Conference on Artificial Intelligence and Statistics*, volume 238 of *Proceedings of Machine Learning Research*, pp. 226–234. PMLR, 2024.

MacKay, D. J. C. A practical Bayesian framework for backpropagation networks. *Neural Computation*, 4(3):448–472, 1992.

Maddox, W. J., Izmailov, P., Garipov, T., Vetrov, D., and Wilson, A. G. A simple baseline for Bayesian uncertainty in deep learning. In *Proceedings of the 33rd Conference on Neural Information Processing Systems (NeurIPS)*, 2019.

Martens, J. and Grosse, R. Optimizing neural networks with kronecker-factored approximate curvature. In *Proceedings of the 32nd International Conference on Machine Learning (ICML)*, 2015.

Rasmussen, C. E. and Williams, C. K. I. *Gaussian Processes for Machine Learning*. MIT Press, 2006.

Roy, H., Miani, M., Ek, C. H., Hennig, P., Pförtner, M., Tatzel, L., and Hauberg, S. Reparameterization invariance in approximate bayesian inference. In *Advances in Neural Information Processing Systems*, 2024.

Sagun, L., Evci, U., Guney, V. U., Dauphin, Y., and Bottou, L. Empirical analysis of the hessian of over-parametrized neural networks. *arXiv preprint arXiv:1706.04454*, 2017.

Sun, S., Zhang, G., Shi, J., and Grosse, R. Functional variational Bayesian neural networks. In *International Conference on Learning Representations*, 2019.

Yu, H., Hartmann, M., Sanchez, B. W. M., Girolami, M., and Klami, A. Riemannian laplace approximation with the fisher metric. In *Proceedings of the 27th International Conference on Artificial Intelligence and Statistics*, 2024.

A. Detailed Methodology

A.1. Background

A.1.1. BAYESIAN NEURAL NETWORKS

Let $\mathcal{D} = \{(x_n, y_n)\}_{n=1}^N$ denote training data, with inputs $x_n \in \mathbb{R}^D$ and outputs y_n in a regression or classification space. A neural network with parameters $\theta \in \Theta \cong \mathbb{R}^K$ defines a function $f_\theta : \mathbb{R}^D \rightarrow \mathbb{R}^C$. A Bayesian neural network places a prior $p(\theta)$ over parameters and defines a likelihood $p(y_n | x_n, \theta)$, leading to a posterior

$$p(\theta | \mathcal{D}) \propto p(\mathcal{D} | \theta) p(\theta) = \left[\prod_{n=1}^N p(y_n | x_n, \theta) \right] p(\theta). \quad (17)$$

Predictions for a new input x_* marginalise over the posterior:

$$p(y_* | x_*, \mathcal{D}) = \int p(y_* | x_*, \theta) p(\theta | \mathcal{D}) d\theta. \quad (18)$$

This integral is intractable in deep networks, motivating approximate inference.

We will assume an isotropic Gaussian prior $p(\theta) = \mathcal{N}(\theta; 0, \lambda^{-1}I)$, corresponding to L_2 weight decay with strength λ .

A.1.2. EUCLIDEAN LAPLACE APPROXIMATION

The Euclidean Laplace approximation (ELA) fits a Gaussian to the posterior around the MAP. Let

$$L(\theta) = -\log p(\theta | \mathcal{D}) = -\log p(\mathcal{D} | \theta) - \log p(\theta) + \text{const.} \quad (19)$$

The MAP estimate is $\theta_{\text{MAP}} = \arg \min_\theta L(\theta)$. Expanding L in a second-order Taylor series around θ_{MAP} gives

$$L(\theta) \approx L(\theta_{\text{MAP}}) + \frac{1}{2}(\theta - \theta_{\text{MAP}})^\top H(\theta - \theta_{\text{MAP}}), \quad (20)$$

where $H = \nabla_\theta^2 L(\theta)|_{\theta_{\text{MAP}}}$ is the Hessian. Exponentiating and normalising yields

$$q_{\text{ELA}}(\theta) = \mathcal{N}(\theta; \theta_{\text{MAP}}, H^{-1}). \quad (21)$$

For deep networks, storing and inverting the full $K \times K$ Hessian is infeasible. Practical implementations approximate H using diagonal, Kronecker-factored (KFAC), low-rank plus diagonal, or last-layer approximations (Daxberger et al., 2021), often based on the Gauss–Newton or Fisher information matrix in place of the exact Hessian.

While ELA is simple and efficient, it makes a strong geometric assumption: that the posterior mass is well captured by a single Gaussian ellipsoid in the *Euclidean* geometry of parameter space. As we discuss next, this is fundamentally misaligned with the geometry of deep network loss landscapes.

A.1.3. LINEARISED LAPLACE APPROXIMATION

The linearised Laplace approximation (LLA) shifts focus from parameter space to function space. Rather than propagating a Gaussian over weights through the full non-linear network, LLA first linearises f_θ around θ_{MAP} :

$$f_\theta(x) \approx f_{\theta_{\text{MAP}}}(x) + J_\theta(x; \theta_{\text{MAP}})(\theta - \theta_{\text{MAP}}), \quad (22)$$

where $J_\theta(x; \theta_{\text{MAP}}) = \nabla_\theta f_\theta(x)|_{\theta_{\text{MAP}}}$ is the Jacobian of the outputs with respect to the parameters.

Assuming a Gaussian posterior $q(\theta) = \mathcal{N}(\theta; \theta_{\text{MAP}}, H^{-1})$, and a Gaussian likelihood for regression, the predictive distribution becomes Gaussian:

$$p(y_* | x_*, \mathcal{D}) \approx \mathcal{N}\left(f_{\theta_{\text{MAP}}}(x_*), J_\theta(x_*) H^{-1} J_\theta(x_*)^\top + \sigma^2 I\right). \quad (23)$$

The first term in the covariance reflects epistemic uncertainty propagated through the Jacobian; the second captures aleatoric noise.

Empirically, LLA often yields better calibrated predictive uncertainty than ELA in deep networks, because it operates in a space that is closer to what we care about: the space of functions rather than raw weights. However, its accuracy relies on the local linearisation being valid; for points far from the training data or along highly non-linear regions of the network, the linear approximation can be poor, and the method effectively behaves like a sophisticated linear model rather than a genuinely non-linear BNN.

For classification tasks, the predictive distribution involves integrating the softmax likelihood under the Gaussian distribution over logits. Since this integral is intractable, common approximations include the analytic Probit method (or moment-matching) and Monte Carlo integration. In our main experiments, we utilize the analytic Probit approximation as the standard efficient baseline for LLA, but we provide a detailed ablation comparing it against Monte Carlo integration in Appendix B.5.1.

A.1.4. RIEMANNIAN GEOMETRY AND FISHER INFORMATION

Information geometry equips parameter spaces of probabilistic models with Riemannian metrics derived from the Fisher information (Amari, 1998). A K -dimensional differentiable manifold M is a space that is locally diffeomorphic to \mathbb{R}^K . At each point $\theta \in M$, the tangent space $T_\theta M$ is a K -dimensional vector space of directions in which one can move infinitesimally.

A Riemannian metric G assigns to each θ a positive definite inner product

$$\langle u, v \rangle_{G(\theta)} = u^\top G(\theta) v, \quad u, v \in T_\theta M, \quad (24)$$

which allows one to measure lengths, angles and geodesic distances. In statistical models, the natural metric is the Fisher information matrix

$$F(\theta) = \mathbb{E}_{p(y|x,\theta)} [\nabla_\theta \log p(y | x, \theta) \nabla_\theta \log p(y | x, \theta)^\top], \quad (25)$$

which measures how sensitive the likelihood is to small changes in θ . Directions v for which $v^\top F(\theta)v \approx 0$ are directions along which the model output is nearly invariant, while directions for which $v^\top F(\theta)v$ is large encode data-sensitive directions.

The Levi–Civita connection induced by G defines parallel transport and geodesics on M , and underpins natural gradient methods (Amari, 1998; Bonnabel, 2013) and geometric approaches to approximate inference.

A.2. Discrete Tubular Construction and Parallel Transport

The core algorithmic challenge in TRL is to construct a sequence of parameter states $\{\gamma_0, \dots, \gamma_T\}$ that accurately traces the one-dimensional valley of approximate invariance while maintaining a consistent transverse coordinate system. This involves solving two coupled geometric problems discretely: geodesic-like integration with potential correction, and parallel transport of the normal bundle.

1. Corrected Spine Update (Valley Tracking). Standard gradient descent follows the steepest path to a local minimum, which may oscillate or diverge from the valley floor if the learning rate is large. Conversely, moving purely along the eigenvector v_{\parallel} with the smallest eigenvalue ignores the non-linear curvature of the manifold. To robustly track the valley, we employ a predictor-corrector scheme. Given the current parameter γ_t , we first take a *tangential prediction step* of length Δs along the valley direction $v_{\parallel,t}$. Then, to prevent drift, we apply a *restorative gradient correction*, but crucially, this correction is projected onto the subspace orthogonal to the motion. The update rule is given by:

$$\gamma_{t+1} = \underbrace{\gamma_t + \Delta s v_{\parallel,t}}_{\text{Predictor}} - \underbrace{\eta_{\text{corr}} (I - v_{\parallel,t} v_{\parallel,t}^\top) \nabla_\theta \mathcal{L}(\gamma_t)}_{\text{Transverse Correction}}, \quad (26)$$

where Δs controls the exploration speed along the invariance manifold and η_{corr} (typically 0.1) acts as a centering force. The projection term $(I - vv^\top)$ ensures that the correction does not accelerate or decelerate the progress along the curve (tangential component is zero), isolating the role of centering from exploration.

2. Discrete Parallel Transport (Frame Bundle). To define a coherent transverse coordinate system across the entire tube, the basis matrix $N_t \in \mathbb{R}^{K \times k_{\perp}}$ must be transported along the spine curve $\gamma(t)$ such that the vectors do not rotate

arbitrarily. In differential geometry, this requires the basis vectors to be parallel transported with respect to the Levi-Civita connection, satisfying $\nabla_{\dot{\gamma}} n_i(t) = 0$. In our discrete setting, we approximate this using a scheme analogous to Schild’s Ladder. Let $v_t = v_{\parallel,t}$ be the tangent vector at step t , and v_{new} be the approximate tangent at step $t + 1$, defined by the secant $v_{new} \propto \gamma_{t+1} - \gamma_t$. To update the basis N_t to N_{t+1} :

1. We first transport the frame rigidly to the new point.
2. We compute the projection of the old basis vectors onto the new tangent direction: $C = v_{new}^\top N_t$.
3. We subtract these components to enforce orthogonality with the new path direction:

$$N'_{t+1} = N_t - v_{new} C. \quad (27)$$

4. Finally, since the subtraction distorts the lengths and angles, we restore the orthonormality of the frame via a QR decomposition:

$$N_{t+1} R = \text{QR}(N'_{t+1}). \quad (28)$$

This procedure ensures that N_{t+1} remains an orthonormal basis for the subspace orthogonal to the spine’s velocity ($N_{t+1}^\top v_{new} = 0$), minimizing artificial “spin” and preserving the intrinsic geometry of the transverse covariance structure.

3. Local Transverse Covariance. With the local coordinate frame established, we quantify uncertainty by projecting the full parameter-space curvature onto the subspace spanned by N_t . This effectively ignores the curvature in the sloppy directions not captured by our low-rank approximation, and assumes a flat prior in the null space of the selected subspace. The projected precision matrix is:

$$H_{\perp,t} = N_t^\top (H_t + \lambda I) N_t, \quad (29)$$

where H_t is the GGN or Hessian approximation. To ensure numerical stability during inversion, we add a small jitter εI_{k_\perp} . The transverse covariance used for sampling is then:

$$\Sigma_{\perp,t} = H_{\perp,t}^{-1} = L_{\perp,t} L_{\perp,t}^\top, \quad (30)$$

where $L_{\perp,t}$ is the lower-triangular Cholesky factor. This formulation allows us to draw samples $z \sim \mathcal{N}(0, I_{k_\perp})$ in the latent space and map them to $\delta\theta = N_t L_{\perp,t} z$, generating the anisotropic “pancake” shape orthogonal to the valley at each step.

A.3. Implicit Curvature via Stochastic Lanczos and Dynamic Batching

For modern deep neural networks such as ResNet-18, the parameter space dimensionality ($K \approx 11 \times 10^6$) prohibits the materialization of the full Hessian matrix H , which would require terabytes of memory. TRL circumvents this bottleneck by computing only the top- k_\perp eigenspace of the Generalized Gauss-Newton (GGN) matrix implicitly using the Lanczos algorithm.

The Lanczos iteration requires only the evaluation of matrix-vector products Hv . We compute these efficiently using Pearlmutter’s trick, which relies on a double backpropagation pass through the computational graph:

$$\text{HVP}(v) = \nabla_\theta (\nabla_\theta \mathcal{L}(\theta) \cdot v). \quad (31)$$

Specifically, given a mini-batch \mathcal{B} , we first compute the gradient $g = \nabla_\theta \mathcal{L}(\theta; \mathcal{B})$ maintaining the computational graph. We then compute the scalar product $p = g^\top v$ and differentiate p with respect to θ again.

Noise Reduction via Batch Buffering. Since the exact GGN requires the full dataset, which is infeasible at each step of the tubular construction, we employ a *stochastic approximation*. Naive stochastic estimates of HVPs on single mini-batches have high variance, which can destabilize the Lanczos iteration (leading to loss of orthogonality in the Krylov subspace). To mitigate this, our implementation uses a **dynamic buffering strategy**: at each spine step t , we fetch a buffer of m mini-batches (typically $m = 10$ to 20) from the data loader. The HVP oracle then operates on the averaged loss over this buffer:

$$\text{HVP}_{buffer}(v) \approx \frac{1}{m} \sum_{i=1}^m \nabla_\theta (\nabla_\theta \mathcal{L}(\theta; \mathcal{B}_i) \cdot v). \quad (32)$$

This approach reduces the variance of the curvature estimate by a factor of $1/m$ while keeping the memory complexity constant ($O(1)$ relative to dataset size), enabling scalable “stochastic geometric tracking” of the valley floor even for large-scale vision transformers or ResNets.

B. Detailed Experimental Setup and Hyperparameters

B.1. Toy Experiments

B.1.1. NOISY SINE REGRESSION

Data & Model. We sample $N = 50$ training points uniformly from $x \in [-6, 6]$ with targets $y = \sin(x) + \epsilon$, where $\epsilon \sim \mathcal{N}(0, 0.1^2)$. The model is a 2-layer MLP (50 units, \tanh) with a linear output and Gaussian likelihood, trained for 200 epochs (Adam, $\text{lr}=10^{-2}$).

B.1.2. TWO-MOONS CLASSIFICATION

Data & Model. We generate $N = 300$ points ($\sigma = 0.1$) using `sklearn.make_moons`. The model is identical to the regression MLP but with a Bernoulli likelihood (sigmoid output), trained for 500 epochs.

B.1.3. HESSIAN AND WEIGHT SCOPE

Baselines (Full-Network & Full-Hessian). Unlike the high-dimensional ResNet experiments, the parameter space of these MLPs is small enough ($D \approx 2,600$) to compute and invert the exact full Hessian matrix. Therefore, for ELA and LLA in these toy experiments, we utilize the Full-Network Laplace approximation with a dense Hessian (using `laplace-torch` with `subset_of_weights='all'` and `hessian_structure='full'`). This ensures that the baselines represent the ideal static Gaussian approximation, isolating the benefit of TRL’s tubular geometry from potential Hessian approximation errors or layer restrictions.

B.1.4. HYPERPARAMETER SELECTION

We performed a grid search to select the geometric parameters $(\Delta s, T, \beta_\perp)$ and rank k_\perp minimizing validation NLL. Table 2 summarizes the search ranges and the optimal configuration selected for each task. Notably, both tasks benefited from a higher rank $k_\perp = 30$ to capture the full local curvature, although the tube scale β_\perp was significantly smaller for regression, reflecting the tighter data constraints.

Table 2. Hyperparameter search space and selected configurations for Toy Experiments.

Parameter	Search Space	Regression (Best)	Classification (Best)
Spine steps (T)	$\{10, 30, 50\}$	30	50
Step size (Δs)	$\{0.01, 0.02, 0.05, 0.08\}$	0.02	0.08
Tube scale (β_\perp)	$\{0.005, 0.01, 0.05, 0.1, 1.0\}$	0.005	0.05
Transverse rank (k_\perp)	$\{2, 3, 5, 8, 10, 30\}$	30	30

B.2. ResNet-18 Details

B.2.1. TRAINING CONFIGURATION

The Maximum A Posteriori (MAP) solution serves as the initialization γ_0 for TRL. We train a standard ResNet-18 using Stochastic Gradient Descent (SGD) with Nesterov momentum (0.9) and a batch size of 128. The initial learning rate is set to 0.1 and decays following a cosine annealing schedule over 50 epochs. Standard weight decay of $\lambda = 5 \times 10^{-4}$ corresponds to an isotropic Gaussian prior during training. Data augmentation includes random cropping (32×32 with padding 4) and horizontal flips.

B.2.2. TRL PRIOR AND SCALE INVARIANCE

Deep networks exhibit scale invariance in weight space, where permutations and scaling of weights across layers leave the function unchanged. This symmetry leads to “flat” directions in the loss landscape and anisotropic curvature, causing standard Gaussian approximations to inflate variance unboundedly. While methods like Riemannian diffusions (Roy et al., 2024) address this by sampling in function space, TRL tackles it directly in parameter space by carefully handling the anisotropic geometry induced by these invariances.

Antorán et al. (2022) further demonstrate that standard marginal likelihood optimization fails in this regime, necessitating layer-wise prior adjustments to properly constrain these invariance directions. To adhere to this recommendation while

avoiding the prohibitive cost and numerical instability of optimizing marginal likelihood for every layer individually in an 11M-parameter network, we adopt a robust two-group layer-wise strategy:

1. **Anchor Point:** We first optimize the prior precision λ_{LL} for the last linear layer using the Laplace approximation ('marglik'), as this subspace is convex and computationally cheap (~ 5000 parameters). This provides a data-driven baseline.
2. **Layer-wise Scaling:** Deep convolutional layers often require stronger regularization to maintain stability than the final linear readout. We introduce a hyperparameter γ_{boost} to define a distinct prior precision λ_{conv} for these layers.
3. **Implementation:** We selected $\gamma_{\text{boost}} = 50$ empirically based on validation performance. We observed that standard priors ($\gamma_{\text{boost}} \approx 1$) failed to counteract the scale invariance, leading to divergent spine trajectories, while significantly larger values overly constricted the posterior. Setting $\lambda_{\text{conv}} = 50 \cdot \lambda_{LL}$ provided a stable regime for the tubular construction.

B.2.3. BATCH NORMALIZATION CONSISTENCY (FixBN).

Standard Bayesian inference on weight space often neglects the interplay between sampled weights and Batch Normalization (BN) statistics. In TRL, parameter samples θ_t can drift significantly from the MAP initialization. We observed that reusing the MAP's frozen BN statistics leads to poor generalization for these samples. Conversely, updating BN statistics during the trajectory construction (validation phase) with augmented data introduces noise. To resolve this, we enforce a strict separation: we freeze BN layers in `eval` mode during the spine construction to maintain a consistent geometry. During inference (sampling), we perform a recalibration pass ("FixBN") using a dedicated dataloader with shuffling and augmentation disabled. This ensures that the activation statistics for each sampled model accurately reflect the training distribution geometry without stochastic noise.

While recalibrating BN statistics requires access to a subset of training data and adds a computational overhead during inference, this practice is standard in modern Bayesian deep learning baselines like SWAG (Maddox et al., 2019) to ensure that weight-space perturbations do not shift internal activation statistics out of the valid regime. For deployment scenarios where training data is inaccessible, one could explore alternative normalization layers (e.g., GroupNorm) or store pre-calibrated BN statistics for each spine point, though we leave this optimization for future work.

B.3. ResNet-18 on CIFAR-10

While the main text focuses on the more challenging CIFAR-100 benchmark, we also extensively validated TRL on CIFAR-10. **Configuration:** We used $k_{\perp} = 20$, $T = 20$, $\Delta s = 0.03$, and $\beta_{\perp} = 1.0$ (selected via validation grid search, Table 4). Batch Normalization statistics were recalibrated on clean training data.

Quantitative Results: Table 3 compares TRL against baselines on CIFAR-10. TRL achieves the lowest calibration error (ECE 0.0063) among single-model methods, confirming the method's effectiveness across datasets of varying difficulty.

Table 3. Full Benchmark on CIFAR-10 (ResNet-18). TRL outperforms single-basin baselines in calibration while maintaining high accuracy.

METHOD	↑ ACC (%)	NLL ↓	ECE ↓	BRIER ↓	OOD AUROC ↑
<i>Training-based Baselines</i>					
SWAG	93.69	0.2040	0.0226	0.0955	0.9477
DEEP ENSEMBLES	95.17	0.1534	0.0073	0.0730	0.9499
MC DROPOUT	91.97	0.2969	0.0406	0.1254	0.8737
<i>Post-hoc Baselines</i>					
MAP	94.32	0.2110	0.0296	0.0910	0.9093
ELA (LAST-LAYER)	94.06	0.3450	0.1676	0.1307	0.9042
LLA-GLM (LAST-LAYER)	94.26	0.1942	0.0215	0.0866	0.9123
TRL (OURS)	94.19	0.1837	0.0063	0.0875	0.9355

It is worth noting that while SWAG achieves a marginally higher OOD AUROC (+1.2%) due to its broader covariance estimation derived from the SGD trajectory, this comes at the cost of significant in-distribution miscalibration (3.5× worse

ECE than TRL). TRL offers a more precise geometric fit, prioritizing strict reliability on valid data while maintaining highly competitive OOD detection.

B.3.1. SENSITIVITY ANALYSIS

We performed a grid search on the held-out validation set (5,000 images) to select the geometric hyperparameters of the tube. Table 4 reports the validation Negative Log-Likelihood (NLL) for various configurations. We observe that the method is remarkably robust: performance remains within a tight NLL band (0.181 – 0.196) across different choices of spine length and step size. The most critical parameter is the transverse scale β_{\perp} ; values $\beta_{\perp} > 1.2$ typically led to under-confidence in the CIFAR-10 setting, while values near 1.0 achieved the optimal balance.

Table 4. Sensitivity Analysis (Validation NLL for ResNet-18). TRL remains stable (NLL $\sim 0.18 – 0.19$) across varying geometric configurations, suggesting the valley structure is robust.

Spine Steps (T)	Step Size (Δs)	Tube Scale (β_{\perp})	Validation NLL	Selected
10	0.05	0.5	0.1883	
10	0.05	1.0	0.1815	
20	0.03	0.5	0.1872	
20	0.03	1.0	0.1814	✓
20	0.05	1.0	0.1959	

Final configuration selected: $T = 20$, $\Delta s = 0.03$, $\beta_{\perp} = 1.0$, $k_{\perp} = 20$. This rank selection is motivated by the well-documented “spiked” nature of the Hessian spectrum in deep neural networks (Maddox et al., 2019). As shown in Figure 3, the eigenvalues of our ResNet-18 exhibit a sharp decay, where the top-20 components capture the majority of the meaningful curvature information (stiff directions). The remaining bulk corresponds to flat or noisy directions that contribute little to the posterior structure, justifying the truncation at $k_{\perp} = 20$.

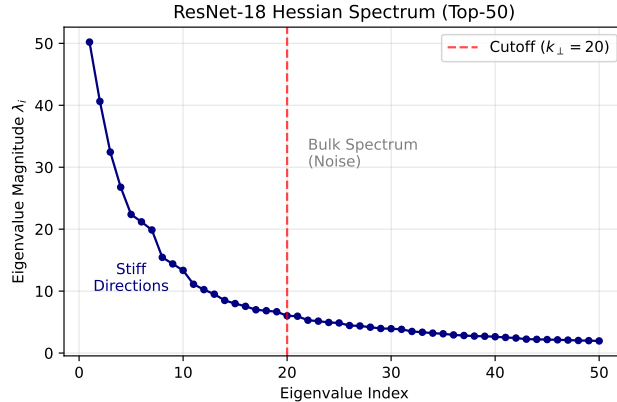


Figure 3. **Empirical Hessian Spectrum (ResNet-18 on CIFAR-10).** Computed via Lanczos iteration on the MAP estimate. The spectrum exhibits a characteristic rapid decay (“spiked” structure). Our choice of $k_{\perp} = 20$ (red dashed line) captures the dominant stiff directions ($\lambda_i > 5$) before the spectrum flattens into the uninformative bulk ($\lambda_i < 5$), balancing geometric fidelity with computational efficiency.

B.4. ResNet-18 on CIFAR-100: Robustness and Hyperparameters

Scaling geometric inference to the 100-class problem required specific algorithmic stabilizations compared to the CIFAR-10 setting.

Robust Gradient Normalization. Standard projected gradient descent steps can lead to numerical explosion when traversing the steep transverse directions characteristic of the CIFAR-100 landscape. To mitigate this, we implemented an RMS-normalized update rule for the correction step. We replace the raw projected gradient g_{\perp} with:

$$g_{\text{step}} = \frac{g_{\perp}}{\sqrt{\text{mean}(g_{\perp}^2) + \epsilon}}, \quad \theta_{t+1} = \theta_t + \Delta s v_{\parallel} - \eta g_{\text{step}} \quad (33)$$

where $\epsilon = 10^{-12}$. This ensures that the centering force η represents a consistent physical step size, acting as adaptive gradient clipping.

Sensitivity Analysis and Grid Search. While $k_{\perp} = 20$ suffices to capture the dominant curvature in CIFAR-10 (as shown in Figure 3), the richer semantic landscape of CIFAR-100 necessitates a higher rank ($k_{\perp} = 30$) to span the relevant subspace of data-constrained directions. We also utilized a spine length of $T = 40$ to capture the complex geometry. The main results are reported in Table 1 (Main Text) where we performed a sweep over the tube scale factor β_{\perp} on the validation set, observing a clear convex basin of optimal performance (Table 5).

Table 5. Sensitivity Analysis on CIFAR-100 Validation Set. We observe a clear optimum at $\beta_{\perp} = 4.0$.

TUBE SCALE (β_{\perp})	VALIDATION NLL
2.0	0.9830
3.0	0.9585
4.0	0.9439

Values significantly lower than 2.0 resulted in underfitting (insufficient exploration), while larger scales destabilized the batch normalization statistics. The optimal scale $\beta_{\perp} = 4.0$ combined with the layer-wise prior strategy described in Appendix B.2 yielded the reported calibration. Note that the optimal scale $\beta_{\perp} = 4.0$ is significantly larger than for CIFAR-10 ($\beta_{\perp} \approx 1.0$), despite using the same regularization strength ($\gamma_{\text{boost}} = 50$). This difference arises from the intrinsic geometry of CIFAR-100: the higher output dimensionality creates a more constrained solution manifold, requiring a larger scaling factor relative to the Hessian-induced width to effectively explore diverse functional behaviors.

B.5. Baseline Implementations

To ensure a rigorous comparison, all baselines employ the exact same ResNet-18 architecture (with the CIFAR-10/100 modified 3×3 kernel) and data split (45,000 training / 5,000 validation) as the TRL experiments.

Laplace Baselines (ELA & LLA) (Daxberger et al., 2021). We utilize the `laplace-torch` library for standard Laplace approximations. To handle the high dimensionality of ResNet-18, we employ the **Last-Layer** approximation, treating the feature extractor as fixed and inferring the posterior only over the weights of the final classification layer.

- **Curvature:** We use the Kronecker-factored (Kron) Generalized Gauss-Newton (GGN) approximation, which provides a better trade-off between memory and accuracy than diagonal approximations.
- **Prior:** The prior precision is optimized via marginal likelihood maximization ('marglik'), ensuring the strongest possible baseline performance without manual tuning.
- **Inference and Approximation Nuances:**
 - **ELA (Euclidean):** We sample weights from the Gaussian posterior and compute the predictive distribution via Monte Carlo integration ($S = 25$ samples).
 - **LLA (Linearised):** We use the standard **Generalized Linear Model (GLM)** formulation with the analytic Probit approximation (MacKay, 1992) to map the Gaussian over logits to probabilities.
- **Remark on LLA Performance:** We distinguish between the standard analytic Probit approximation (LLA-GLM) and Monte Carlo predictive integration (LLA-MC). Our ablation (Appendix B.5.1) shows that on CIFAR-10, the analytic Probit is stable. However, on CIFAR-100 under marginal-likelihood prior selection, the Probit mapping becomes inaccurate due to the large posterior scale. While replacing it with Monte Carlo integration (as used in ELA and LLA-MC) improves robustness, static last-layer Laplace still remains significantly worse than TRL in this regime. This confirms that the dominant limitation is the single local Gaussian posterior assumption.

Deep Ensembles (Lakshminarayanan et al., 2017). We trained $M = 5$ independent models with different random initializations. Each model was trained for 50 epochs using SGD (lr = 0.1, momentum = 0.9, cosine annealing), identical to the MAP baseline. Predictions are averaged over the 5 models. This represents the gold standard for uncertainty but requires 5× training and inference cost.

SWAG (Diagonal) (Maddox et al., 2019). We implemented Stochastic Weight Averaging-Gaussian (SWAG) with a diagonal covariance approximation. The model was trained for a total of 50 epochs. We started collecting weight statistics at epoch 30 (after the initial high-learning rate phase), using a constant learning rate of 0.01 for the collection phase. At inference time, we sampled $S = 25$ models from the Gaussian posterior and performed Batch Normalization recalibration on the training subset for each sample before averaging predictions.

MC Dropout (Gal & Ghahramani, 2016). We modified the ResNet-18 architecture to include a Dropout layer ($p = 0.1$) before the final linear layer. The model was trained with dropout enabled. At inference time, we performed $S = 25$ stochastic forward passes with dropout active to estimate the predictive distribution.

B.5.1. ABLATION: ANALYTIC PROBIT VS. MONTE CARLO INTEGRATION FOR LLA

In classification, the predictive distribution requires integrating a softmax likelihood under a Gaussian distribution over logits. The standard LLA baseline (denoted LLA-GLM) uses an efficient closed-form Probit approximation. To verify that our conclusions are not an artifact of this analytic mapping, we additionally evaluate **LLA-MC**, which performs Monte Carlo predictive integration under the same marginal-likelihood optimized prior ($S = 25$ samples).

Table 6 presents the comparison. On CIFAR-10, LLA-GLM (Probit) performs strongly and is stable. LLA-MC yields similar results, while ELA performs worse in this specific setting. However, on CIFAR-100 (high uncertainty), the Probit mapping degrades substantially under marginal likelihood optimization (NLL 1.4182). Replacing it with Monte Carlo integration improves LLA significantly (NLL 1.2818), bringing it close to ELA’s performance.

Crucially, even with robust MC integration, static last-layer Laplace baselines remain far worse than TRL (NLL ≈ 0.95) in this high-dimensional regime. This confirms that TRL’s performance gains are driven by its superior tubular geometry, rather than just the choice of predictive integration method.

Table 6. Ablation study of Laplace inference methods (Prior optimized via MargLik). LLA-GLM (Probit) fails on CIFAR-100 but excels on CIFAR-10. LLA-MC is robust but still underperforms TRL. *Note: numbers are from a single run; small differences w.r.t. main tables can arise from random seed and finite Monte Carlo estimation ($S=25$)*

METHOD	CIFAR-10		CIFAR-100	
	NLL \downarrow	ECE \downarrow	NLL \downarrow	ECE \downarrow
ELA (MC)	0.3462	0.1683	1.2952	0.2407
LLA-GLM (PROBIT)	0.1939	0.0209	1.4182	0.3378
LLA-MC (MONTE CARLO)	0.2130	0.0219	1.2818	0.2359
TRL (OURS)	0.1837	0.0063	0.9525	0.0171

C. Full Toy Experiment Results (Full-Network Baselines)

C.1. Noisy sine regression

Our first experiment is a one-dimensional noisy regression problem. Inputs $x \in [-6, 6]$ are sampled uniformly and targets are generated as

$$y = \sin(x) + \varepsilon, \quad \varepsilon \sim \mathcal{N}(0, 0.1^2). \quad (34)$$

We train a two-layer tanh MLP with 50 hidden units (under a Gaussian likelihood) by maximum a posteriori (MAP) optimisation and fit a full Laplace approximation using `laplace-torch`. For evaluation we draw Monte Carlo samples from each approximate posterior and compute predictive statistics on a dense test grid.

Table 7 reports root mean squared error (RMSE), NLL and calibration diagnostics based on

$$z_n = \frac{y_n - \mu_n}{\sigma_n}, \quad (35)$$

where μ_n and σ_n^2 are the predictive mean and variance at the n -th test point. For a well-calibrated Gaussian predictive distribution we expect $\text{Var}(z_n) \approx 1$ and empirical coverage of $|z_n| \leq 1, 2, 3$ close to the nominal 68.3%, 95.5%, 99.7%.

Euclidean Laplace (ELA) essentially fails on this problem: its predictive mean does not recover the sinusoidal structure and its uncertainty bands are extremely wide, leading to a very poor NLL (3.90) and a z -variance close to zero, indicating

Table 7. Noisy sine regression. RMSE and NLL on the test grid, and z –statistics. Lower is better for RMSE and NLL; z –variance and coverages are ideal when close to the Gaussian targets.

Method	RMSE	NLL	z –var	$\text{cov}_{1\sigma}$
ELA	0.87	3.90	0.002	1.00
LLA	0.37	0.95	0.051	1.00
TRL	0.26	0.03	0.32	0.93

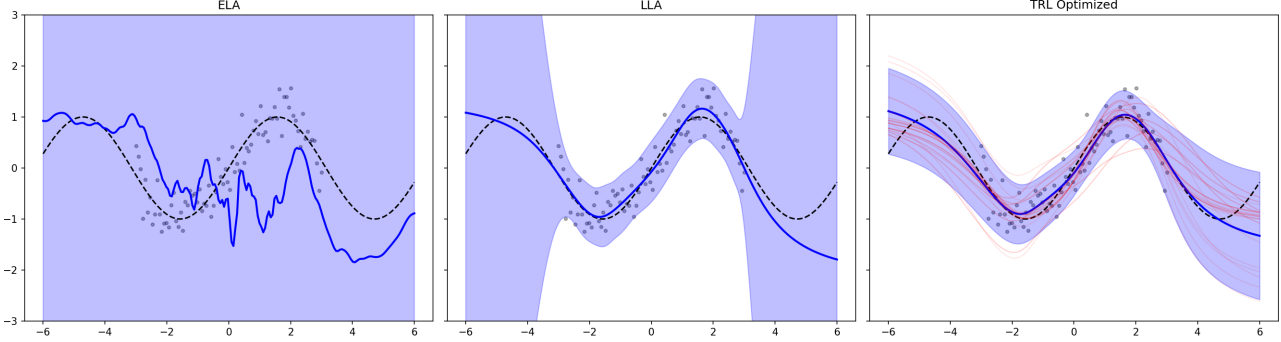


Figure 4. Noisy sine regression. Predictive mean (blue) and two–sigma bands (shaded) for Euclidean Laplace (left), linearised Laplace (middle) and TRL with Hessian–based valley and parallel transport (right). The dashed black curve is the ground–truth sine.

that the predictive variance has been grossly over–estimated. The linearised Laplace approximation (LLA) substantially improves the fit: it recovers the correct shape of the sine and reduces the NLL to 0.95. However, LLA remains strongly over–conservative: the predictive variance is still too large (again z –variance $\ll 1$ and 100% coverage at 1σ), so that almost all points fall well inside the nominal confidence bands.

TRL, in contrast, achieves both the lowest RMSE (0.26) and an NLL that is two orders of magnitude smaller (0.03). The predictive mean closely tracks the underlying sine wave, and the uncertainty bands tighten significantly around the data while still expanding in regions without observations. The z –variance (0.32) and 1σ coverage (93%) show that TRL is still mildly conservative, but much closer to the ideal Gaussian behaviour than ELA or LLA. Visually (Figure 4), the TRL tube averages out small oscillations along the loss valley and produces a smooth, well–calibrated ensemble of functions, whereas ELA and LLA either underfit or inflate uncertainty everywhere.

Crucially, the z –variance of 0.32 for TRL indicates that, despite the tighter uncertainty bands seen in Figure 4, the method is not overconfident on the test distribution. In fact, a z –variance below 1.0 suggests the model remains slightly conservative (over-dispersed) relative to the true noise, but it corrects the extreme under-confidence of ELA and LLA. This confirms that TRL’s tubular geometry successfully captures the necessary posterior mass to explain the data without inflating variance in well-supported regions.

C.2. Two–moons classification

Our second experiment is a binary classification task on the two–moons dataset. We generate 300 points with noise level 0.1 and train the same two–layer tanh network (50 hidden units) with a Bernoulli likelihood. The Laplace approximation again uses a full Hessian at the MAP; ELA samples logits directly from the Gaussian weight posterior, whereas LLA propagates uncertainty through a linearisation of the logits around the MAP. TRL uses the same practical Hessian–based valley construction as in the regression experiment, with hyperparameters given by the tuned configuration above.

Table 8 reports negative log–likelihood (NLL) and Brier score, using Monte Carlo estimates of the predictive probability $p(y = 1 \mid x)$ for each method.

Euclidean Laplace again performs poorly: the classifier is barely better than random (accuracy ≈ 0.54 , not shown in the table), and its predictive probabilities collapse towards 0.5 across most of the input space, yielding a Brier score close to that of a constant $p = 0.5$ predictor. The corresponding entropy map (Figure 5, top left) shows high uncertainty almost everywhere.

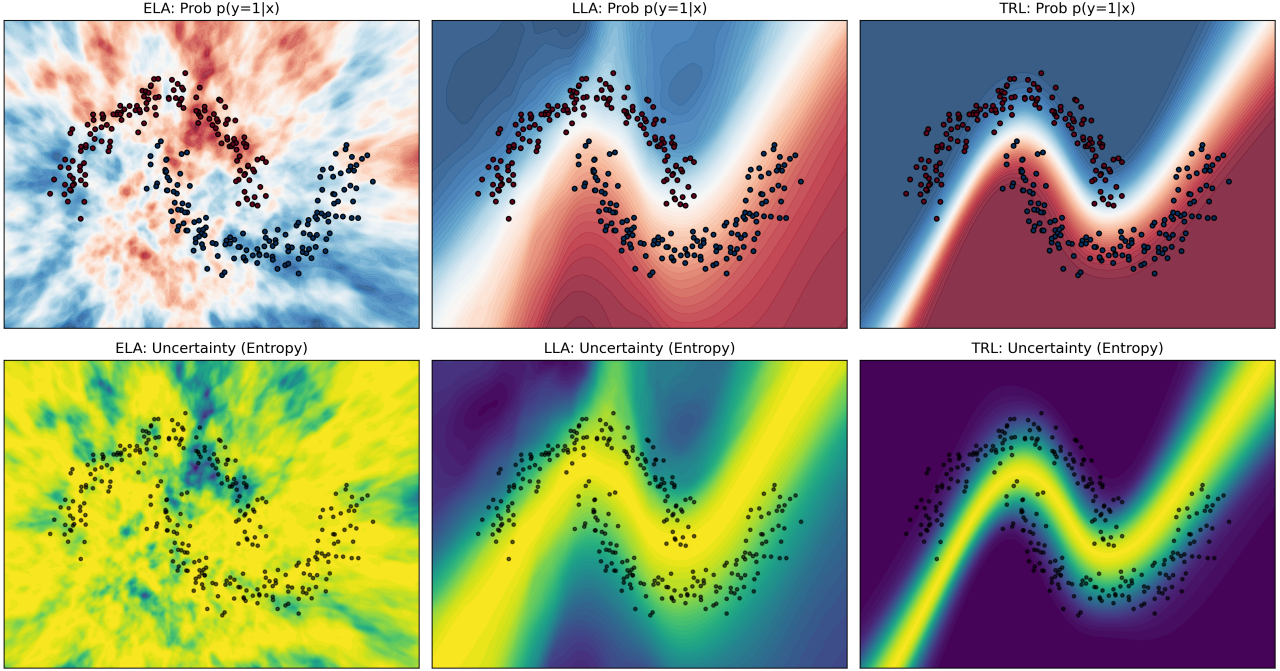


Figure 5. Two-moons classification. Top row: predictive probability $p(y = 1 | x)$ for ELA (left), LLA (middle) and TRL (right). Bottom row: corresponding predictive entropy. Black dots are training points. TRL produces sharp, well-aligned decision regions and concentrates uncertainty along the class boundary and far from the data.

Table 8. Two-moons classification. Negative log-likelihood (NLL) and Brier score on the full dataset. Lower is better.

Method	NLL	Brier
ELA	0.67	0.239
LLA	0.39	0.108
TRL	0.09	0.015

LLA dramatically improves accuracy (the MAP decision boundary is recovered and accuracy reaches 100%), but the model remains under-confident: typical probabilities along each moon are around 0.6–0.7, leading to an NLL of 0.39 and a Brier score of 0.11. The entropy plot (bottom middle in Figure 5) shows elevated uncertainty spread over large regions of the space, including areas far from the data manifold.

TRL matches the perfect accuracy of LLA while achieving a much lower NLL (0.09) and Brier score (0.015). The probability map (top right in Figure 5) shows that TRL assigns probabilities very close to 0 or 1 on the interior of each moon, with uncertainty tightly concentrated along the decision boundary and in regions far from the training data. The entropy map (bottom right) confirms this selective uncertainty: entropy is low on clearly classified points and high only where ambiguity is expected. In other words, TRL not only predicts the correct labels but also attaches the right level of confidence to those predictions.

It is important to interpret these sharp decision boundaries correctly. While TRL visually resembles the MAP estimate more than the diffuse “cloud” of LLA, the superior NLL and Brier scores (Table 8) demonstrate that this confidence is well-calibrated for the data distribution. Unlike function-space methods that may enforce high entropy globally away from data points, TRL allows the neural network’s inductive bias to extrapolate structural invariances (the valley). This yields high confidence where the learned symmetries hold, avoiding the under-confidence on valid data often observed in linearized or Euclidean baselines.

D. Computational Complexity and Sampling Efficiency

A fundamental advantage of TRL over prior Riemannian Laplace Approximations (RLA) lies in the decoupling of the geometric analysis phase from the sampling phase. Here we provide a detailed breakdown of the computational complexity.

D.1. ODE-based RLA (Standard Approach)

Methods such as Bergamin et al. (2023) and Yu et al. (2024) define the posterior implicitly via geodesic flows. To generate S samples from the posterior, one must solve an Initial Value Problem (IVP) for a second-order ODE for *each* independent sample.

- **Process:** For each sample $s = 1 \dots S$:

1. Sample an initial velocity $v^{(s)} \sim \mathcal{N}(0, G^{-1}(\theta_0))$.
2. Integrate the geodesic equation component-wise for T_{int} steps:

$$\frac{d^2\theta_k}{dt^2} + \sum_{i,j} \Gamma_{ij}^k \frac{d\theta_i}{dt} \frac{d\theta_j}{dt} = 0,$$

where Γ_{ij}^k are the Christoffel symbols derived from the metric $G(\theta)$.

- **Computational Bottleneck:** Although practical implementations employ approximations to make the ODE tractable, the inference cost remains high. Bergamin et al. (2023) use a Monge metric to avoid third derivatives, but still require running a numerical integrator for T_{int} steps per sample, necessitating multiple gradient evaluations. Yu et al. (2024) aim for higher fidelity using the Fisher metric and volume corrections, which introduces the additional (and often prohibitive) cost of estimating log-determinant gradients. In both cases, the iterative nature of the solver scales linearly with the number of samples S , creating a latency bottleneck.
- **Total Inference Cost:** $O(S \cdot T_{\text{int}} \cdot C_{\text{curv}})$, where C_{curv} denotes the cost of evaluating the metric tensor (and potential log-determinant terms) at each integration step. Crucially, this cost scales linearly with S . If real-time uncertainty requires $S = 30$ samples, the heavy geometric computation must be repeated 30 times, creating substantial latency during inference.

Similar complexity constraints apply to Riemannian diffusion approaches like Roy et al. (2024), which require solving Stochastic Differential Equations (SDEs) during inference, incurring comparable iterative costs.

D.2. TRL (Ours): Amortized Geometry

TRL bypasses the repeated solution of ODEs by making a structural assumption: the posterior mass concentrates along a low-loss valley. This allows us to shift the heavy lifting to a "pre-computation" phase.

- **Construction Phase (Fixed Cost):** We construct the spine $\{\gamma_t, N_t, L_{\perp,t}\}_{t=1}^T$ once. This involves solving the predictor-corrector updates and running Lanczos iterations.
 - Cost: $O(1 \cdot T_{\text{spine}} \cdot C_{\text{lanczos}})$.
 - **Amortization:** This cost is incurred only once per trained model, regardless of how many millions of samples are eventually drawn in deployment. In our experiments, T_{spine} is a small constant (20–40 steps), with larger values used for more complex datasets (e.g., CIFAR-100).
- **Inference Phase (Sampling):** To generate S samples, we perform no geometric integration. We simply map latent noise through the pre-computed structure:
 1. Sample latent $z \sim \mathcal{N}(0, I_{k_{\perp}+1})$.
 2. Apply the linear map: $\theta^{(s)} = \gamma_t + N_t(L_{\perp,t}z_{\perp})$.
- **Inference Cost:** $O(S \cdot K \cdot k_{\perp})$ for sampling, plus the cost of FixBN. Since N_t is a tall-skinny matrix ($K \times k_{\perp}$), the sampling operation consists of cheap matrix-vector products. Importantly, no backpropagation or expensive curvature evaluations are required during inference (only standard forward passes for prediction and FixBN recalibration).

Storage vs. Training Trade-off. While TRL significantly reduces training cost ($1 \times$ MAP optimization) compared to Deep Ensembles ($5 \times$), it incurs a storage overhead to maintain the discretized spine $\{\gamma_t\}_{t=1}^T$. For a spine of length $T = 40$, this requires storing T parameter vectors, whereas an ensemble stores $M = 5$. However, this storage cost is strictly linear $O(T)$ and concerns disk space/RAM, which is typically abundant compared to the prohibitively expensive GPU hours required to train multiple independent models. Furthermore, techniques like quantization or storing only weight deltas can mitigate this overhead in deployment.

TRL effectively shifts the geometric complexity from *inference time* (online) to *training time* (offline). While standard RLA methods must "re-discover" the local curvature for every particle via expensive integration, TRL "paves the road" once and travels it cheaply. This design enables TRL to combine the non-linear geometric fidelity of Riemannian approaches with an inference throughput comparable to Euclidean approximations (ELA/LLA), offering a practical alternative to computationally intensive ODE-based sampling.